PAPER

Droplet generation in cross-flow for cost-effective 3D-printed "plug-and-play" microfluidic devices†

Jia Ming Zhang,[a] Andres A. Aguirre-Pablo,[a] Er Qiang Li,[a] Ulrich Buttner[b] and Sigurdur T. Thoroddsen*[ac]

Droplet-based microfluidics is a rapidly growing field of research and involves various applications from chemistry to biology. Droplet generation techniques become the pre-requisite focus. Additive manufacturing (3D printing) technology has recently been exploited in microfluidics due to its simplicity and low cost. However, only relatively large droplets can be produced in current 3D-printed droplet generators, due to the channel dimension limitations on how fine a channel can be 3D-printed. Here we report a novel design of a 3D-printed "plug-and-play" device for the generation of monodisperse microdroplets with sizes down to ~50 μm. This device combines a 3D-printed generator, a commercial tubing and a fingertight fitting, which can be easily assembled and disassembled. Different emulsions, water-in-oil and oil-in-water, can be generated in the same device. Scaling laws for droplet sizes generated in our device have been successfully proposed and verified. Furthermore, the feasibility of 3D printing technology used in droplet-based engineering applications has been demonstrated by two novel 3D-printed devices, as well as by using the device for producing magnetically responsive microparticles.

1 Introduction

Since droplet-based microfluidics provide the feasibility of handling small volumes of fluids conveniently, its applications have grown substantially in the past decades.[1] This has opened up the development of novel applications in physics, chemistry and biology.[2–5] Exploiting efficiently the benefits of droplet-based microfluidics requires a deep understanding of droplet generation, control and handling in the related devices. A variety of fabrication techniques of microfluidic devices for droplet generation have been reported,[6] which primarily involve hot embossing[7] and soft lithography.[8] In both cases, two or more individual layers are bonded together to form a complete chip. The fabrication process typically involves cleanroom microfabrication, followed by molding and bonding of different layers, which requires complicated manual operations and is quite time consuming due to this multi-step process. Another common method for fabrication of droplet-based microfluidic devices is assembly of glass capillary devices.[9] Tapered glass capillaries are easily made and can be surface treated for controlling wettabilities, which is necessary for producing multiple emulsions. Different tapered glass capillaries can be assembled to produce complex multiple emulsion droplets or microbubbles.[10,11] However, glass capillaries need to be tapered using a micropipette puller and also need to be assembled manually, which hinders their mass production, or routine usage in lab or industry. Recently, many simple strategies have been proposed to fabricate microfluidic devices for emulsion generation. Various coaxial flow-focusing capillary devices have been successfully applied to generate emulsions.[12–18] Benson *et al.*[19] designed a focusing capillary device that could be disassembled and cleaned between uses. Martino *et al.*[20] reported a design where the tip distance between capillaries can be adjusted, which enables tuning the droplet breakup regimes. Deng *et al.*[21,22] cut and patterned glass coverslips to form microchannels for emulsion generation.

In recent years, three dimensional (3D) printing technology has been through a rapid development and has attracted extensive attention from the microfluidics community.[23] With 3D printing, the time needed for fabrication is greatly reduced, as the process can be completed with a single printing machine, in a single step and being fully automated. In addition, 3D printing is capable of creating complex 3D structures, while only planar structures can be produced with current commonly used methods. Compared to other methods, the material cost of

[a]Division of Physical Sciences and Engineering, King Abdullah University of Science and Technology (KAUST), Thuwal, 23955-6900, Saudi Arabia. E-mail: sigurdur.thoroddsen@kaust.edu.sa

[b]Division of Computer, Electrical and Mathematical Sciences and Engineering, King Abdullah University of Science and Technology (KAUST), Thuwal, 23955-6900, Saudi Arabia

[c]Clean Combustion Research Center, King Abdullah University of Science and Technology (KAUST), Thuwal, 23955-6900, Saudi Arabia

† Electronic supplementary information (ESI) available: S1. W/O emulsion generation. S2. O/W emulsion generation. S3. Larger emulsion generation at the tubing back. S4. Smallest emulsion generation. S5. Emulsion generation with different concentrations. S6. Emulsion droplet coalescence. S7. Design files for printing. S8. Testing the consistency of printed gap distance. See DOI: 10.1039/c6ra11724d

a 3D-printed chip may not be the lowest. However, considering the equipment cost (a micro-pipette puller for capillary microfluidics, for example) and the involved training and practice in fabrication, the manufacturing process in our study is relatively easier. Due to the limitation of production capacity, the mass-production using 3D-printing technique for industry still remains elusive. Its fast prototyping ability is more suitable for customized products, such as experimental chips used in lab for proof of concept. The high cost of printers once hindered exploitation of 3D printing technology in microfluidics, but in the last few years, several low-cost 3D printers have emerged on the market. This has allowed researchers to readily develop various 3D-printed microfluidic devices, such as microfluidic automation devices,[24] microdissectors,[25] and electrochemical detection devices.[26] The use of CAD models to produce devices gives the user ability to integrate parts in a plug and play manner, and a couple of strategies for 3D-printed integrated devices have been developed.[27–29]

However, the benefits of 3D printing of microfluidic devices have not yet been exploited in droplet-based microfluidics. Only a handful of studies on droplet generation in 3D-printed devices have been reported using low-cost desktop 3D printers.[30–32] One of the major limitations of this technology is the difficulty of removing the uncured resin or other support materials from small channels due to the capillary effect. Although the layer resolution of current desktop printers can achieve 50 μm or even finer, the actually printed channel dimension (feature size) has so far only reached 250–350 μm using current commercial resins in the best case,[33] which can be an order of magnitude larger compared to the resolution of the printer itself. Furthermore, this channel cannot be long or has a complex geometry, since this will increase the risk of channel clogging due to uncured materials which become more difficult to remove. The disadvantage of having a relatively wide 3D-printed channel, is that it is not capable of producing droplet sizes as small as those produced by conventional microfluidic devices.[34] This hinders the full implementation of 3D printing technology in droplet-based microfluidics. Recently, Gong *et al.*[35] formulated a customized resin to reach the minimum dimensions of ∼60 μm channels, but the resin was opaque and no functional printed parts were reported in their work. This shows great promise, but an advanced and expensive 3D printer with higher layer resolution is required to achieve this dimension.

Herein we propose a novel design of 3D-printed hybrid "plug-and-play" device for the generation of monodisperse droplets with sizes comparable to those generated in current microfluidic devices. The device consists of a 3D-printed channel with an embedded screw thread to connect a commercial fitting. This fitting holds an inserted commercial tubing that can be easily replaced. The inserting depth of the tubing can be accurately controlled by our design. By combining the tubing with the channel, the effective feature size of our device can reach down to ∼100 μm with 100% yield. This is the smallest size achieved in current 3D-printed microfluidic devices produced by desktop devices. Different emulsions, water-in-oil (W/O) and oil-in-water (O/W), can be generated using different tubings. Furthermore, the feasibility of this 3D printing technique for use in droplet-based applications is demonstrated by introducing two plug-and-play 3D-printed microfluidic devices.

2 Methods

The 3D-printed microfluidic devices were designed using Solidworks (Dassault Systemes S.A.), and then printed with a low-cost desktop printer Form 1+ (Formlabs, Inc.). This desktop printer is based on the stereolithography (SLA) technique to build structures[36] and only costs $2799, which is affordable and could become widespread in most laboratories. A major advantage of SLA is the high feature resolution, provided by the process of photo-curing a resin with a UV laser. This makes SLA a good candidate for fabrication of droplet-based microfluidic devices since a smooth channel surface is crucial for droplet creation and transportation inside the microchannel. Another benefit of SLA lies in the availability of a clear resin, which provides an excellent transparency after being polished appropriately, thus, allowing researchers to observe the internal fluid flow such as droplet generation. This is crucial for many microfluidic applications requiring optical access. This clear resin contains modified acrylate oligomer and monomer, together with a photoinitiator but their weight ratio is proprietary.

In addition, the Young's modulus of the postcured clear resin is 2.7 Gpa, which is much larger than that of PDMS: 0.75×10^{-3} Gpa. Therefore, our devices, printed with this material, are capable of withstanding higher liquid flow rate and input pressure, which leads to benefits such as the increase of the droplet generation frequency and reduction of the droplet sizes through larger viscous stress.

The basic design of our device is illustrated in Fig. 1(a) and (b). A screw-thread was designed to allow the connection of a commercial 1/16 inch fingertight cone fitting in order to hold a commercial tubing (1/16 inch OD and 0.007 inch ID), through which the dispersed phase flows. A flat and smooth tubing surface is preferred for droplet formation. Such surface can be achieved using a low-cost commercial tube cutter to cut the tubing, followed by polishing the end surface with a fine sand paper (grit size of FEPA P2400). Following the thread, a conical structure was added to the design for sealing this cone fitting. Next, a tubing chamber was added to accommodate the commercial tubing. This chamber is cylindrical with diameter 1/16 inch (∼1.6 mm), matched to the tubing OD. The tubing is inserted into this chamber, enclosed by the fitting. The final height of chamber depends on our design, which determines the tubing position inside the main channel. This main channel with a square cross-section has a width of 1 mm, through which the continuous phase is introduced. The depth to which the tubing is inserted into the channel, is controlled by a 3D-printed ledge against which the tubing-end butts, as shown in Fig. 1(a) and (b). Finally, the dispersed phase pinches off in this small gap between the tubing and the channel wall. The channel can be printed in relatively large dimensions with little effects on droplet size, since droplets are generated in the small gap instead of the main channel. While printing the device, the
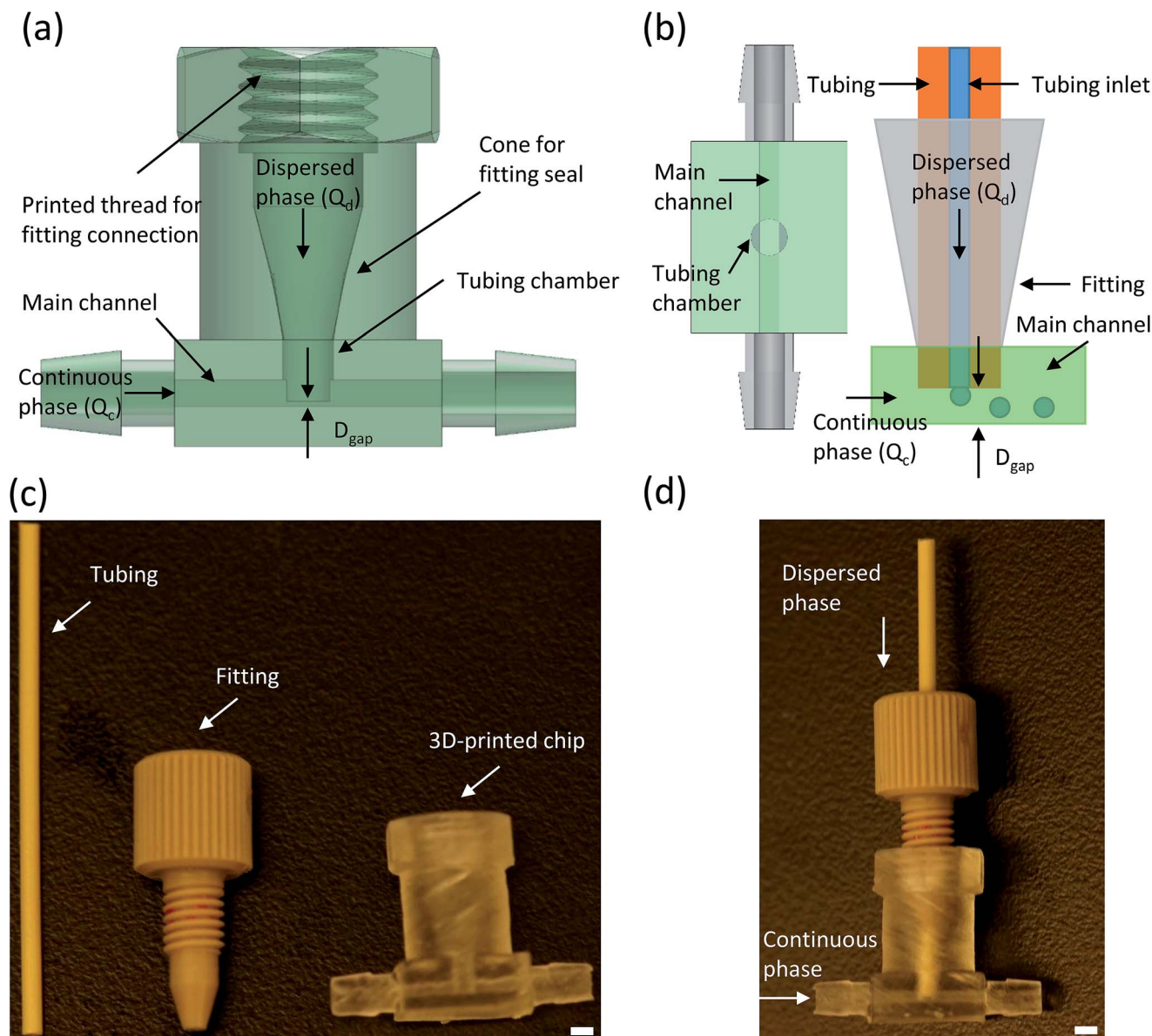
Fig. 1 Schematic of a 3D-printed emulsion generator with (a) side view, (b) bottom view and schematic of droplet generation with an inserting tubing. The dispersed phase (Q_D) is introduced through a tubing with a fingertight fitting connected within the printed thread. The continuous phase (Q_c) flows in the main channel. The droplet is generated in a small gap with designed height 300 μm. (c) A commercial tubing (1/16 inch OD) and a fingertight fitting along side the 3D-printed chip. (d) Assembly of the full device consisting of the tubing, the fitting and the 3D-printed generator. Both scale bars are 1 mm.

chamber structure works as a vent for releasing uncured resin, making it easy to clean from any unwanted residues. Our design overcomes the limitation of having a minimum channel size between 250 and 300 μm. The dimension of small gap is limited by the height of the ledge which is determined by the layer resolution of our desktop 3D-printer, *i.e.* 100 μm. All design files are given in the ESI, S7,† and these files can be directly used in 3D-printers.

Silicone oils (Sigma-Aldrich) with different viscosities were used as the continuous oil phases, and water–glycerin mixtures of different viscosities were used as the dispersed aqueous phases. Tetradecane (Sigma-Aldrich) was used as the dispersed oil phase. Red dyes were applied in the aqueous phase to

enhance observability, as well as Sudan red used for the same purpose in the oil phase. The surfactant Tween 20 (Sigma-Aldrich) was used in the aqueous phase, and the surfactant Dow Corning 749 (Dow Corning Corp.) was used in the oil phase. The interfacial tension between aqueous phases and oil phases were measured using a tensiometer (Kruss GmbH), the values for all the liquids used in the present study are listed in Table 1. The difference of interfacial tension between specific water/glycerin mixture with different viscosities of silicone oils is negligible, but different viscosities of water–glycerin mixtures slightly influence the interfacial tension. Here 100 cSt silicone oil was used for measuring the interfacial tension with different viscosities of water–glycerin mixtures.

Table 1 Liquids used in the experiments

Aqueous phase (water/glycerin mixture)	Oil phase (silicone oil)	Different viscosity pair of liquids	Interfacial tension value (σ) (mN m^{-1})
1 cP	50 cSt	1 cP to 100 cSt	20
10 cP	100 cSt	10 cP to 100 cSt	19
100 cP	350 cSt	100 cP to 100 cSt	18

The commercial fittings and tubings as shown in Fig. 1(c) were purchased from IDEX Corporation. Syringe pumps (Fusion 200, Chemyx, Inc.) were applied for driving the liquids into the devices. The formation processes of the droplets were observed and recorded with a high-speed color CMOS video camera (Photron SA-3). The sizes of the droplets were analyzed using the free image-analysis software ImageJ. Since the dimension of the main channel is 1 mm, which is much larger than the droplet sizes generated in all experiments, the droplets have little deformation in the main channel and we assume their shape is spherical. All experiments were carried out at room temperature of 22 °C.

3 Results and discussion

3.1 The generation of different emulsions

Since the droplets are generated from the opening of the inserted tubing, its surface wettability is crucial for producing different emulsions (W/O or O/W). One tubing was treated to make it hydrophobic using a commercial coating agent (Glaco Mirror Coat 'Zero', Soft 99 Co.),[37] to allow generation of W/O emulsion, as shown in Fig. 2(a) and S1.† The other tubing was treated to become hydrophilic using oxygen plasma, to generate O/W emulsion, as shown in Fig. 2(b) and S2.† Both W/O and O/W emulsions were produced in a highly monodisperse manner. One benefit with this setup is that only the tubing needs to be replaced for producing different emulsions and the channel wall does not need surface treatment. Thus, different emulsions can be generated in the same microfluidic generator without additional surface treatment.

3.2 Flow-pattern

In the present study, the flow pinch-off dynamics occurred in the dripping regime. Unlike in the microfluidic T-junctions,[38] the jetting regime is observed in other studies.[39,40] There is no jetting regime in our device even when the flow rate of dispersed phase is large. Instead of the jetting regime, the dispersed phase will attach to the tubing surface and flow to the back area of the tubing, where a stable liquid cone is formed and pinches off to generate monodisperse droplets with larger sizes, as shown in Fig. 2(c) and S3.† The velocity of the continuous phase flow at the backside of the tubing is much lower than that in the gap, and thus less viscous stresses are exerted on the dispersed phase in this area. So larger droplets were generated during pinch-off in the tubing back area. This novel regime is beyond the scope of the present study and will not be discussed in details here.

3.3 Geometry effects

The geometric parameters including the tubing inside diameter (ID) and the gap distance (D_{gap}) influence the droplet sizes. Smaller droplets can be produced with smaller tubing ID or smaller D_{gap}.[41] The main channel dimension has little influence on the drop sizes because the droplet are generated in the gap area instead of the main channel. The droplets were all generated with the same tubing ID ($D_{tubing} = 177$ μm) in the present study. Owing to the transparency of our channel, the actual gap distance can be precisely measured in video frames captured by a camera. As shown in Fig. 2(d), the gap distance we obtained here is 262 μm, compared with the design distance 300 μm. The actual channel dimension is usually smaller than the design
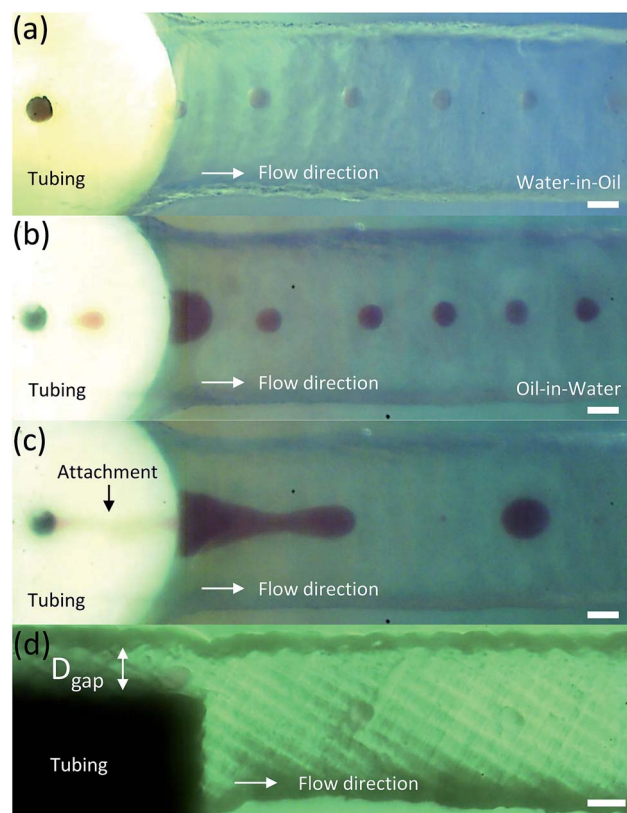

Fig. 2 Droplet generation in our 3D-printed device. (a) Aqueous droplet generation. (b) Oil droplet generation. (c) The dispersed phase attaches to the tubing wall due to the large flow rate of the dispersed phase. (d) Side view of the printed device. The printed gap distance (D_{gap}) is 262 μm with the designed gap distance 300 μm. All scale bars are 200 μm.

due to incomplete removal of the filler resin residues. The reproducibility of the printed gap distance can be ensured by this printing technique and more details are given in the ESI, S8.† The smallest D_{gap} with 100% yield, using our low-cost desktop printer Form 1+, is 115 μm, with the design distance of 150 μm. It is close to the layer resolution we set in this 3D-printer. Droplets with a diameter of ~50 μm can be generated with this smallest gap distance even if the tubing ID is much larger than the droplet sizes, as is shown in the S4.† Such small gap induces much larger shear, which favors the pinch-off the dispersed phase to generate smaller droplets.

3.4 Fluid analysis

W/O emulsions are used for the fluid analysis in the following section. Besides using different viscosities of continuous phases, different viscosities of dispersed phases were also used for altering the viscosity ratio in the present study. The droplet size (D) was scaled by the tubing ID (D_{tubing}) and thus we obtain the dimensionless droplet size ($D_{\text{drop}} = D/D_{\text{tubing}}$). First, we investigated the effects of flow rate ratio (Q_d/Q_c) on the droplet sizes. As shown in Fig. 3, the droplet sizes increase overall with increasing the flow rate ratio. In other words, when the flow rate of the continuous phase is reduced, the droplets become larger.

At the same flow rate ratio, smaller droplets were generated with a more viscous continuous phase, which is consistent with other studies. Surprisingly, smaller droplets were also generated with more viscous dispersed phase. The experimental results show that not only the viscosity ratio has influence on the droplet size, but the viscosity of dispersed phase can also affect the droplet size. The reason for the variation of the droplet size with different viscosity ratio is still unclear. For a higher viscosity of the continuous phase, more viscous stresses are exerted on the droplet interface with the same flow rate ratio. Thus, the dispersed phase is more easily pinched off and causes smaller droplets to be generated. Few studies have reported the effects of the viscosity of the dispersed phase on droplet sizes. Higher liquid viscosity can result in greater deformation, which stretches out the dispersed phase from the tubing into a filament before this filament ruptures. Therefore, a smaller portion of the liquid supply results in the smaller droplets.

The droplet pinch-off process results from the balance of the viscous stresses, interfacial tension and squeezing pressure.[42] The capillary number Ca describes the relative magnitude of the viscous forces compared with the interfacial forces. Here we define Ca in terms of the average velocity (u_c) of the continuous phase flow within the narrow gap:

$$\text{Ca} = \frac{\mu_c u_c}{\sigma} = \frac{\mu_c Q_c}{\sigma D_{\text{gap}} w} \qquad (1)$$

where μ_c is the viscosity of the continuous phase, σ is the interfacial tension and w is the main channel width, $w = 1$ mm in all experiments. D_{gap} is the gap distance between the tubing and channel wall, and $D_{\text{gap}} = 262$ μm. We plot D_{drop} as a function of Ca in Fig. 4. As shown in Fig. 4, the droplet sizes decrease with increasing Ca. This trend is consistent with other studies on microfluidic T-junctions.[39,42] We observe the variation of the droplet sizes with Ca over the entire range (10^{-2} to 10^0) in our experiments. In Fig. 4, we find that the droplet size exhibits a power-law dependence on Ca. For dispersed phase of 1 cP and 10 cP, the exponents are −0.33 and −0.27 respectively. This agrees with the value given in other studies in microfluidic T-junctions, where the exponent is ~−1/3.[42,43] But for the most viscous dispersed phase of 100 cP, the curve has a larger slope with an exponent of −0.44. This demonstrates that the exponent is not a uniform value for different viscosities of dispersed
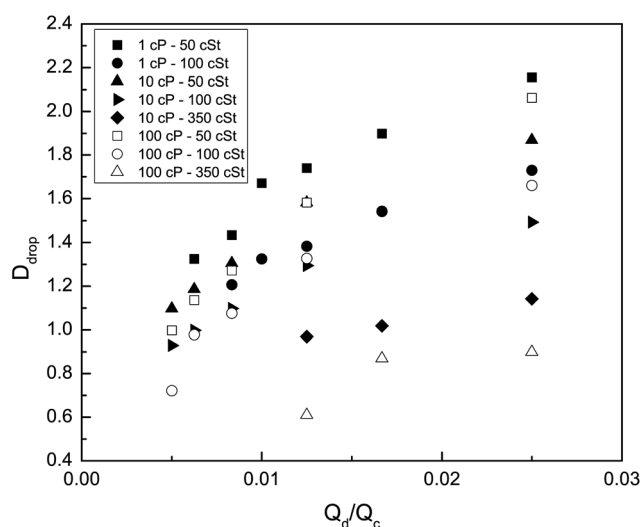

Fig. 3 Dimensionless droplet size with variation of flow rate ratio. The dispersed flow rate (Q_d) is kept constant at 5 μL min^{-1}. The continuous flow rate (Q_c) is altered from 200 μL min^{-1} to 1000 μL min^{-1}. The drop sizes increase with increasing the flow rate ratio, *i.e.* when the flow rate of the continuous phase is reduced, the droplet becomes larger.
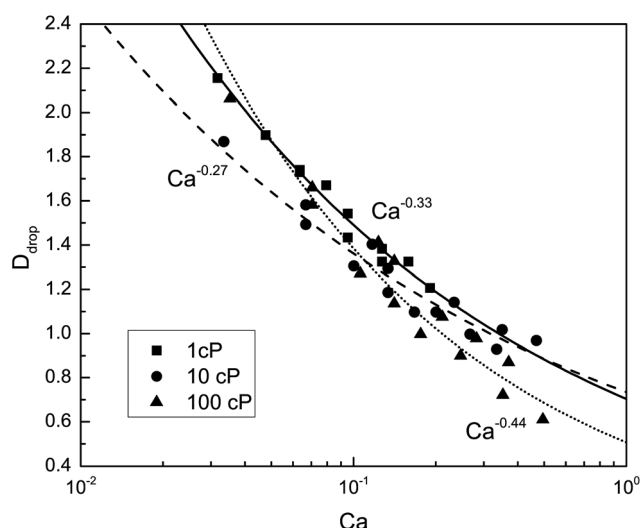

Fig. 4 Dimensionless droplet size as a function of capillary number with different viscosities of the dispersed and continuous phases. The dispersed phase used here is 1 cp, 10 cP and 100 cP, respectively. The continuous phase used here is 50 cSt, 100 cSt and 350 cSt for each viscosity of the dispersed phase. Note that the curve for the 100 cP dispersed phase has a larger slope.

phases. For a higher viscosity of the dispersed phase, the exponent deviates from $\sim-1/3$ to $\sim-1/2$. No studies have reported this deviation yet.

The flow rate ratio in Fig. 3 goes up to 0.025 and higher flow rate ratio is investigated in the Fig. 5: Q_c was kept constant as 200 μL min^{-1} and the viscosity of the continuous phase was kept constant as 350 cSt. The flow rate of the dispersed phase is increased from 10 μL min^{-1} to 50 μL min^{-1}, which makes the flow rate ratio higher. In Fig. 5, we plot D_{drop} against flow rate ratio. It shows the droplet size increases linearly with an increment of the flow rate of the dispersed phase. Droplet sizes depend not only on the flow rate ratio, but also on the absolute flow rate of the dispersed phase. The curve for the higher viscosity dispersed phase has a larger slope. More specifically, the droplet sizes exhibit a linear relation dependence on the flow rate ratio. Notice that over the range of flow-rate ratios in Fig. 5, the droplet sizes exceed the gap distance (D_{gap}). This is similar to the squeezing regime reported in microfluidic T-junction.[40] The droplet starts to block the continuous phase flow in the gap in the vertical direction, and the squeezing pressure plays a role in this regime. In this case, the droplet sizes therefore mainly depend on the flow rate ratio instead of Ca.

Few studies on droplet generation frequency in microfluidic T-junctions have been reported.[39,42] In Fig. 6, we plot the droplet generation frequency as a function of flow rate ratio with different viscosity ratio of the liquid phases. At the same flow rate ratio, more viscous continuous phase or more viscous dispersed phase cause larger generation frequency. From the view of mass conservation, one can calculate the frequency if Q_d and the droplet size are known. We see that smaller droplets are generated with more viscous continuous phase or with more viscous dispersed phase. Thus, the higher generation frequency
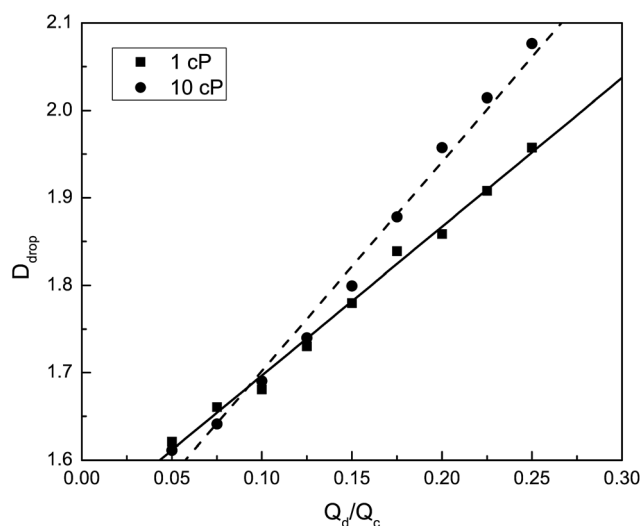

Fig. 6 The frequency of droplet generation as a function of flow rate ratio for different viscosities of the dispersed and continuous phases. All curves are power-laws with exponents in a narrow range, from −1.1 to −1.4.

results from the smaller droplet sizes when the flow rate of the dispersed phase is constant. In addition, in Fig. 6, we find that the droplet generation frequency exhibits a power-law dependence on the flow rate ratio. The power-law exponent lies in a narrow range from −1.1 to −1.4, as shown in Fig. 6.

4 Applications

One major advantage of 3D printing technology is to allow researchers to design and integrate different functional parts in a modular manner. Therefore, we have designed and fully 3D-printed two functional parts which can be integrated with our droplet generator for further droplet-based applications. These functional parts were also printed with our low-cost desktop printer, as introduced in the following section.

4.1 Parallel droplet generation with different concentrations

The concentration of reagents is one of the most important parameters in chemical or biological libraries,[44] but the ability to control and vary the concentration of reagents still remains a challenge in microfluidic research.[45] To vary the concentration usually requires complex fluid networks, which must be integrated with other functional structures in the same layer of the chip. Due to current planar fabrication methods, it is not possible to integrate too many channels in one layer. Thus, multilayered chips have been needed to achieve multiple functions. However, the increased complexity of the fabrication introduces potential problems, as any single defective part can disable the whole chip.

Here we have designed and 3D-printed a simple single-level gradient concentration generator as shown in Fig. 7. This generator is integrated with the droplet generator to demonstrate the feasibility of producing droplets with different concentrations, which is of great potential for chemical

Fig. 5 Dimensionless droplet size with variation of flow rate ratio. Q_d is altered from 10 μL min^{-1} to 50 μL min^{-1}, while Q_c is kept constant at 200 μL min^{-1}. The viscosity of the continuous phase is kept constant at 350 cSt and the viscosity of the dispersed phase used here is 1 cP and 10 cP, as marked by the different symbols. Note that the curve for the higher viscosity of dispersed phase has a larger slope.
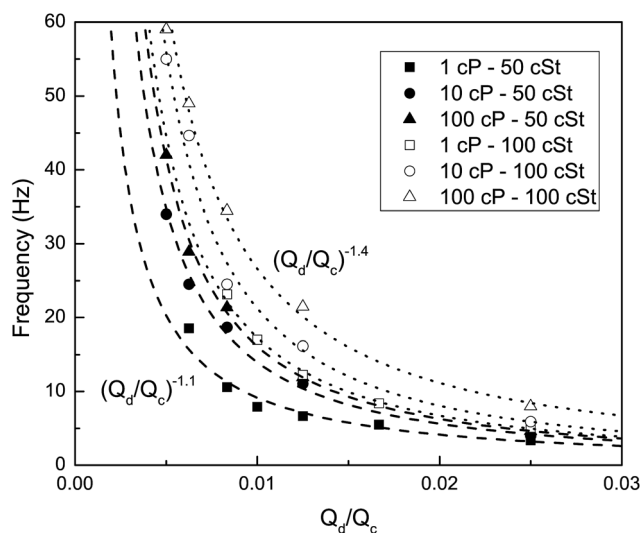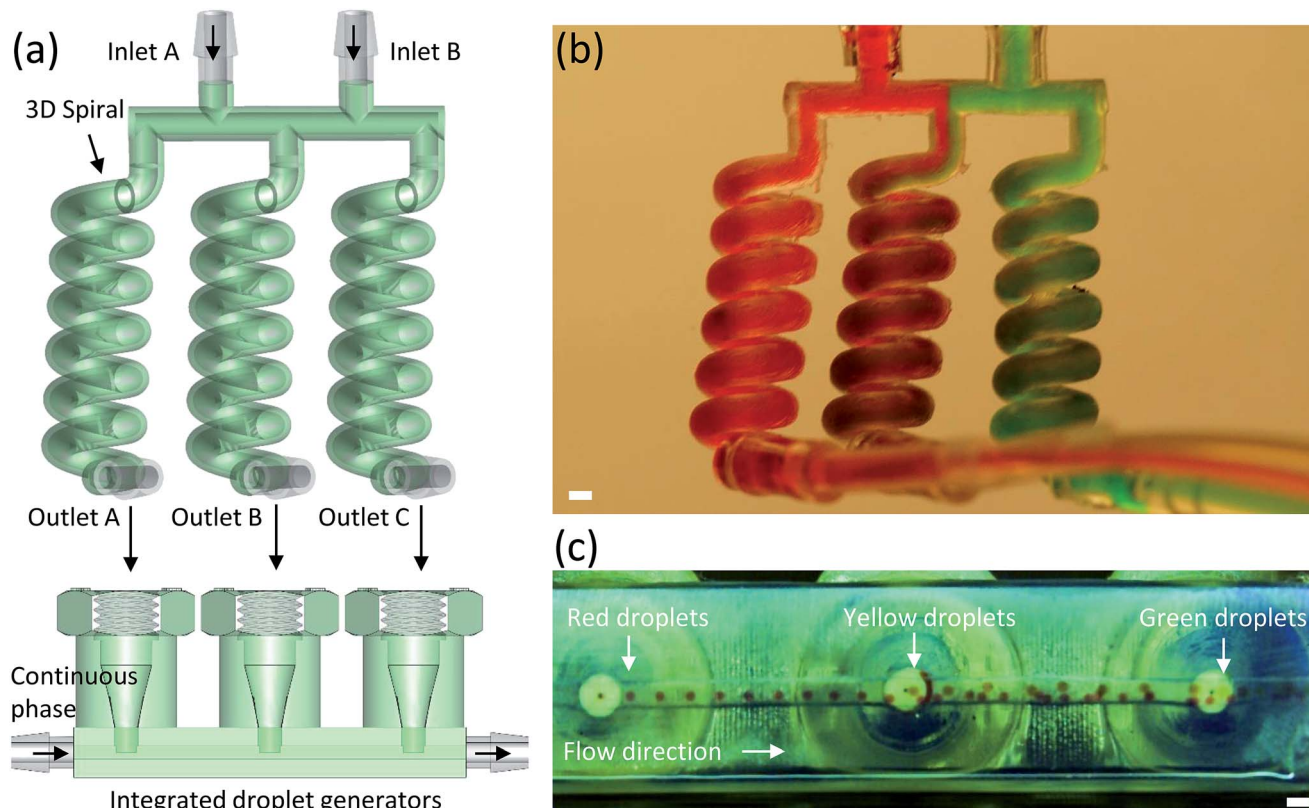
RSC Advances

Paper

Fig. 7 (a) Schematic of a 3D-printed gradient concentration generator. 3D spirals facilitate mixing. (b) The printed gradient concentration generator. 10 cP water/glycerin mixtures with red and green dyes were introduced through two inlets, respectively. (c) Video frame of droplet generation with different color (red, yellow and green). Both scale bars are 1 mm.

reactions and drug testing.[46,47] The 3D-printed coil channels can enhance liquid mixing compared to planar strategies. As shown in Fig. 7(b), 10 cP water/glycerin mixtures with red and green dyes were introduced through two separate inlets. The red and green liquids keep their concentration in both side spiral channels while the red and green liquids are mixed in a central spiral channel, resulting in a yellow liquid at the exit. Then these three liquid streams are used as the dispersed phases in three parallel droplet generators to produce a stream of droplets with different concentrations, here represented by three colors: red, yellow and green, as shown in Fig. 7(c) and S5.† Multiple-level gradient concentration generator can also be printed by simple extension of more levels for obtaining more complex gradients and gradient distribution. Since the generation of both, concentration and droplet, is modularly independent, it is straightforward for researchers to integrate these two parts for producing droplets with various sizes and concentration differences between droplets.

4.2 Droplet merging

Coalescence or merging of droplets is an important subject in microfluidics due to its wide usage in chemical and biological analyses.[48] Several techniques have been reported to merge droplets.[49] The primary passive strategy of merging droplets involves an expanding channel which facilitates the drainage of the continuous phase between neighboring droplets. But such expansions also introduce more freedom of droplet motion, which increases uncertainty of droplet coalescence.

Here we have designed and printed a 3D coalescence device for merging droplets passively, as shown in Fig. 8(a). The total height of the channel is 1 mm and the height of pillar blocks is 500 μm, which form a gap to allow the continuous phase to flow above them. These pillar blocks form a meandering channel to guide droplet motion. The channel is put in horizontal and gravity keeps the slightly heavier water droplets moving in this meandering channel. In addition, top expanding areas were designed on both sides of the channel to form an expanding chamber for allowing the continuous phase to flow. Therefore, the continuous phase between neighboring droplets is drained in both horizontal and vertical directions. On the other hand, the meandering channel limits the freedom of drop motion. Both, extra drainage of the continuous phase and limited drop motion, greatly facilitates the droplet merging. As shown in Fig. 8(c) and S6,† two droplets (one green and the other red) from two droplet generators move through the meandering channel and they approach each other due to the drainage of the continuous phase in this channel. Finally these droplets merge repeatedly at the end of the channel. The coalescence process of one pair of droplets is also shown in Fig. 8(d). In this case, no surfactants were used.
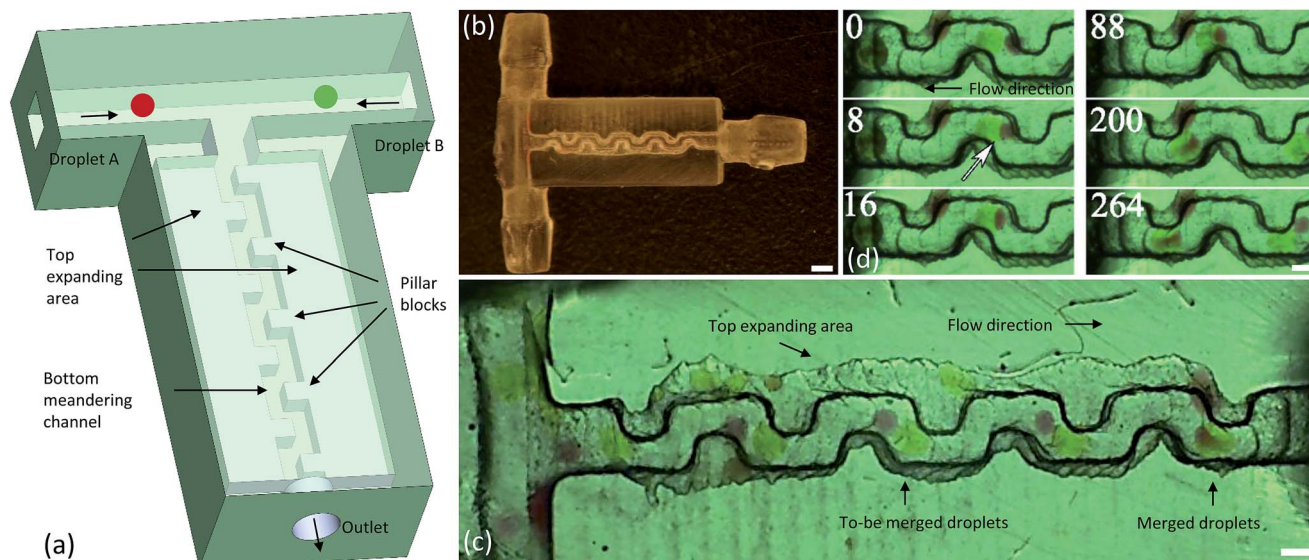
Fig. 8 (a) Schematic of a 3D-printed droplet-merging device. (b) The printed droplet-merging device. Scale bar is 1 mm. (c) High-speed video frame of the droplet coalescence process. (d) Sequence of video frames showing the droplet coalescence process. The arrow shows the starting time point of the coalescence. Numbers show times in ms. Both scale bars in (c) and (d) are 500 μm.
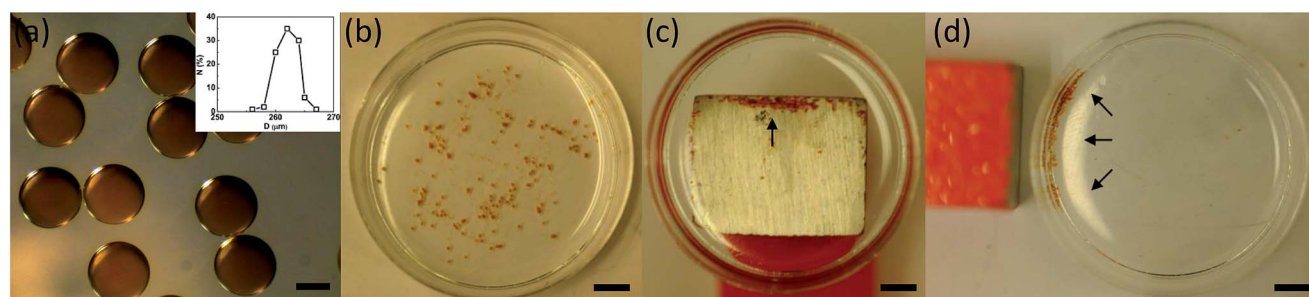

Fig. 9 (a) Microphotograph of magnetically responsive microparticles. The inset shows the size distribution of these microparticles. Scale bar is 150 μm. (b) Magnetically responsive microparticles are dispersed in silicone oil without an applied magnetic field. (c) These microparticles are aligned in a line with a bottom external magnetic field. (d) The microparticles are attracted to the left edge of the Petri dish by a left external magnetic field. Scale bars in (b), (c) and (d) are 5 mm.

4.3 Fabrication of functional microparticles

One of the important applications for microdroplets is to produce functional microparticles. Highly monodisperse microparticles can be produced *via* the microfluidic technique. Magnetically responsive microparticles are widely used in biological and medical engineering.[50–52] Here we demonstrated the capability of emulsion templates produced in our device to fabricate magnetically responsive microparticles. Isobornyl acrylate (IBA) precursor solution (Sigma-Aldrich), together with 5% (v/v) 20 nm nanomagnetic particles solution (Micromod Partikeltechnologie GmbH) and 2 wt% 2,2-dimethoxy-2-phenylacetophenone (Sigma-Aldrich) as photoinitiator were used as the dispersed phase, and 10 cSt silicone oil with surfactants (Dow Corning 749) was used as the continuous phase. Droplets containing nanomagnetic particles were collected in a Petri dish and then exposed under a UV light for 10 seconds, to form magnetically responsive microparticles. Fig. 9 shows the magnetically responsive microparticles and

their movements attracted by a magnet. The inserted image in Fig. 9 shows the particle size distribution generated based on emulsion templates. Monodisperse microparticles can be fabricated through droplet-microfluidic techniques.

5 Conclusion

In the present study, we have designed and 3D-printed a hybrid "plug-and-play" microfluidic droplet generator and two droplet-based application devices. Commercial tubings were used for the dispersed phase input, and also for creating the small gap used for generating the smaller droplet. A screw thread was printed for connecting the fitting which holds the commercial tubing sufficiently tight for droplet generation without leakage. The tubing can be easily replaced with different tubing ID or surface wettabilities, to generate various sizes of emulsion droplets (W/O and O/W).

Subsequently, we performed scaling analysis on the droplet sizes and generation frequencies in our devices, to guide other users using such devices to fulfill their requirements. We find that the droplet sizes depend on liquid flow rate ratio, Ca, and viscosity ratio, which is consistent with other studies in microfluidic T-junctions. But the scaling law is a little different due to differences in our geometric structures. In addition, the experimental results show that the viscosity of the dispersed phase itself can also influence the droplet sizes and frequency of generation.

When the drop size is smaller than the gap distance, the drop generation mainly depends on the viscous forces. The drop size shows a power-law dependence on the Ca in this case. On the other hand, when the drop size is larger than the gap distance, the drop generation mainly depends on the squeezing pressure. In this case, the drop size shows a linear relationship with flow rate ratio.

Finally, we have designed and 3D-printed a gradient concentration generator for droplets of different concentrations, which can be beneficial for chemical reactions and drug testing. In addition, we also made a droplet merging device for droplet coalescence and mixing, which can be useful in chemical and biological applications. Furthermore, magnetically responsive microparticles are produced with our device, which shows the feasibility of our device for engineering applications.

We demonstrate that not only droplet generators can be fabricated using 3D printing technology, but more complex devices can be 3D-printed in a modular way and integrated with the droplet generator to achieve more complex functions based on droplet templates. We envision more such droplet-based applications being developed using 3D printing technology in the future.

Acknowledgements

References

1 G. M. Whitesides, *Nature*, 2006, **442**, 368–373.
2 A. B. Theberge, F. Courtois, Y. Schaerli, M. Fischlechner, C. Abell, F. Hollfelder and W. T. Huck, *Angew. Chem., Int. Ed.*, 2010, **49**, 5846–5868.
3 D. T. Chiu, R. M. Lorenz and G. D. Jeffries, *Anal. Chem.*, 2009, **81**, 5111–5118.
4 J. I. Park, A. Saffari, S. Kumar, A. Günther and E. Kumacheva, *Annu. Rev. Mater. Res.*, 2010, **40**, 415–443.
5 B. G. Chung, K.-H. Lee, A. Khademhosseini and S.-H. Lee, *Lab Chip*, 2012, **12**, 45–59.
6 G. S. Fiorini and D. T. Chiu, *BioTechniques*, 2005, **38**, 429–446.
7 H. Becker and U. Heim, *Sens. Actuators, A*, 2000, **83**, 130–135.
8 Y. Xia and G. M. Whitesides, *Annu. Rev. Mater. Sci.*, 1998, **28**, 153–184.
9 A. S. Utada, E. Lorenceau, D. R. Link, P. D. Kaplan, H. A. Stone and D. A. Weitz, *Science*, 2005, **308**, 537–541.
10 E. Q. Li, J. M. Zhang and S. T. Thoroddsen, *J. Micromech. Microeng.*, 2013, **24**, 015019.
11 J. M. Zhang, E. Q. Li and S. T. Thoroddsen, *J. Micromech. Microeng.*, 2014, **24**, 035008.
12 L.-Y. Chu, A. S. Utada, R. K. Shah, J.-W. Kim and D. A. Weitz, *Angew. Chem., Int. Ed.*, 2007, **46**, 8970–8974.
13 S.-Y. Teh, R. Lin, L.-H. Hung and A. P. Lee, *Lab Chip*, 2008, **8**, 198–220.
14 S. Marre and K. F. Jensen, *Chem. Soc. Rev.*, 2010, **39**, 1183–1202.
15 W. Wang, R. Xie, X.-J. Ju, T. Luo, L. Liu, D. A. Weitz and L.-Y. Chu, *Lab Chip*, 2011, **11**, 1587–1592.
16 S.-H. Kim and D. A. Weitz, *Angew. Chem., Int. Ed.*, 2011, **50**, 8731–8734.
17 P. Wu, Y. Wang, Z. Luo, Y. Li, M. Li and L. He, *Lab Chip*, 2014, **14**, 795–798.
18 Y. Wang, P. Wu, Z. Luo, Y. Li, M. Liao, Y. Li and L. He, *RSC Adv.*, 2014, **4**, 31184–31187.
19 B. R. Benson, H. A. Stone and R. K. Prud'homme, *Lab Chip*, 2013, **13**, 4507–4511.
20 C. Martino, S. Berger, R. C. Wootton, *et al.*, *Lab Chip*, 2014, **14**, 4178–4182.
21 N.-N. Deng, Z.-J. Meng, R. Xie, X.-J. Ju, C.-L. Mou, W. Wang and L.-Y. Chu, *Lab Chip*, 2011, **11**, 3963–3969.
22 Z.-J. Meng, W. Wang, X. Liang, W.-C. Zheng, N.-N. Deng, R. Xie, X.-J. Ju, Z. Liu and L.-Y. Chu, *Lab Chip*, 2015, **15**, 1869–1878.
23 C. M. B. Ho, S. H. Ng, K. H. H. Li and Y.-J. Yoon, *Lab Chip*, 2015, **15**, 3627–3637.
24 A. K. Au, N. Bhattacharjee, L. F. Horowitz, T. C. Chang and A. Folch, *Lab Chip*, 2015, **15**, 1934–1941.
25 E. C. Spivey, B. Xhemalce, J. B. Shear and I. J. Finkelstein, *Anal. Chem.*, 2014, **86**, 7406–7412.
26 J. L. Erkal, A. Selimovic, B. C. Gross, S. Y. Lockwood, E. L. Walton, S. McNamara, R. S. Martin and D. M. Spence, *Lab Chip*, 2014, **14**, 2023–2032.
27 K. C. Bhargava, B. Thompson and N. Malmstadt, *Proc. Natl. Acad. Sci. U. S. A.*, 2014, **111**, 15013–15018.
28 K. G. Lee, K. J. Park, S. Seok, S. Shin, J. Y. Park, Y. S. Heo, S. J. Lee, T. J. Lee, *et al.*, *RSC Adv.*, 2014, **4**, 32876–32880.
29 S. Tsuda, H. Jaffery, D. Doran, M. Hezwani, P. J. Robbins, M. Yoshida and L. Cronin, *PLoS One*, 2015, **10**, e0141640.
30 L. Donvito, L. Galluccio, A. Lombardo, G. Morabito, A. Nicolosi and M. Reno, *J. Micromech. Microeng.*, 2015, **25**, 035013.
31 T. Femmer, A. Jans, R. Eswein, N. Anwar, M. Moeller, M. Wessling and A. J. Kuehne, *ACS Appl. Mater. Interfaces*, 2015, **7**, 12635–12638.
32 J. M. Zhang, E. Q. Li, A. A. Aguirre-Pablo and S. T. Thoroddsen, *RSC Adv.*, 2016, **6**, 2793–2799.
33 A. I. Shallan, P. Smejkal, M. Corban, R. M. Guijt and M. C. Breadmore, *Anal. Chem.*, 2014, **86**, 3124–3130.
34 S. L. Anna, *Annu. Rev. Fluid Mech.*, 2016, **48**, 285–309.
35 H. Gong, M. Beauchamp, S. Perry, A. T. Woolley and G. P. Nordin, *RSC Adv.*, 2015, **5**, 106621–106632.

36 B. Wendel, D. Rietzel, F. Kühnlein, R. Feulner, G. Hülder and E. Schmachtenberg, *Macromol. Mater. Eng.*, 2008, **293**, 799–809.

37 I. U. Vakarelski, N. A. Patankar, J. O. Marston, D. Y. Chan and S. T. Thoroddsen, *Nature*, 2012, **489**, 274–277.

38 T. Thorsen, R. W. Roberts, F. H. Arnold and S. R. Quake, *Phys. Rev. Lett.*, 2001, **86**, 4163.

39 M. De Menech, P. Garstecki, F. Jousse and H. Stone, *J. Fluid Mech.*, 2008, **595**, 141–161.

40 P. Garstecki, M. J. Fuerstman, H. A. Stone and G. M. Whitesides, *Lab Chip*, 2006, **6**, 437–446.

41 K. Wang, Y. Lu, J. Xu, J. Tan and G. Luo, *AIChE J.*, 2011, **57**, 299–306.

42 G. F. Christopher, N. N. Noharuddin, J. A. Taylor and S. L. Anna, *Phys. Rev. E: Stat., Nonlinear, Soft Matter Phys.*, 2008, **78**, 036317.

43 K. Wang, Y. C. Lu, J. H. Xu, J. Tan and G. S. Luo, *AIChE J.*, 2011, **57**, 299–306.

44 A. J. deMello, *Nature*, 2006, **442**, 394–402.

45 D.-K. Kang, X. Gong, S. Cho, J.-y. Kim, J. B. Edel, S.-I. Chang, J. Choo and A. J. deMello, *Anal. Chem.*, 2015, **87**, 10770–10778.

46 N. Damean, L. F. Olguin, F. Hollfelder, C. Abell and W. T. Huck, *Lab Chip*, 2009, **9**, 1707–1713.

47 P. Eribol, A. Uguz and K. Ulgen, *Biomicrofluidics*, 2016, **10**, 011502.

48 I. Shestopalov, J. D. Tice and R. F. Ismagilov, *Lab Chip*, 2004, **4**, 316–321.

49 H. Gu, M. H. Duits and F. Mugele, *Int. J. Mol. Sci.*, 2011, **12**, 2572–2597.

50 B. H. McNaughton, K. A. Kehbein, J. N. Anker and R. Kopelman, *J. Phys. Chem. B*, 2006, **110**, 18958–18964.

51 J.-B. Mathieu and S. Martel, *Biomed. Microdevices*, 2007, **9**, 801–808.

52 D.-S. Xiang, G.-P. Zeng and Z.-K. He, *Biosens. Bioelectron.*, 2011, **26**, 4405–4410.